MATERIALS SCIENCE

Flexible active-matrix organic light-emitting diode display enabled by MoS_2 thin-film transistor

Minwoo Choi,[1]* Yong Ju Park,[1]* Bhupendra K. Sharma,[1] Sa-Rang Bae,[2] Soo Young Kim,[2]† Jong-Hyun Ahn[1]†

Atomically thin molybdenum disulfide (MoS_2) has been extensively investigated in semiconductor electronics but has not been applied in a backplane circuitry of organic light-emitting diode (OLED) display. Its applicability as an active drive element is hampered by the large contact resistance at the metal/MoS_2 interface, which hinders the transport of carriers at the dielectric surface, which in turn considerably deteriorates the mobility. Modified switching device architecture is proposed for efficiently exploiting the high-*k* dielectric Al_2O_3 layer, which, when integrated in an active matrix, can drive the ultrathin OLED display even in dynamic folding states. The proposed architecture exhibits 28 times increase in mobility compared to a normal back-gated thin-film transistor, and its potential as a wearable display attached to a human wrist is demonstrated.

INTRODUCTION

Recently, to realize intelligent electronic systems, there is an increasing demand to combine functional features such as ultrathin characteristics (*1*, *2*), large area (*3*), wrapping onto irregular surfaces (*4*, *5*), easy attachment to the human body (*6*, *7*), and several other characteristics (*8*, *9*) with the current electronic circuitry. Compared to other typically investigated organic (*10*, *11*) and inorganic materials (*12*), van der Waals materials with atomic thickness demonstrate the immense potential for these systems (*13*). Transition metal dichalcogenides such as MoS_2 and WSe_2 with a two-dimensional (2D) atomic layer have been reported to be superior to conventional materials owing to their exceptional electrical and mechanical properties (*14*–*16*). On the basis of their outstanding properties, these materials can be exploited for large-area flexible switching-based applications. In particular, the active-matrix backplane for flexible organic light-emitting diode (OLED) displays is one of the most promising applications of these 2D semiconductors because they offer important benefits such as high carrier mobility, high optical transmittance, and low flexural rigidity required for switching OLEDs on a flexible substrate compared to conventional inorganic semiconductors. Although a few studies have demonstrated the switching of a single-pixel OLED using mechanically exfoliated 2D materials as the semiconducting channel of a thin-film transistor (TFT) (*17*, *18*), these capabilities have not been investigated in flexible systems or in the active-matrix backplane circuitry for large-area OLED displays. Exfoliated monolayer MoS_2 exhibits excellent field-effect mobility (10 to 40 $cm^2\ V^{-1}\ s^{-1}$), but it is not a suitable method for real electronic applications (*10*). Large-area MoS_2 films prepared using chemical vapor deposition (CVD) have been considered as a more favorable candidate for OLED displays, although they exhibit low mobility that results from small grain size, inherently rendering its semiconducting features inferior to those of the exfoliated materials (*19*). However, MoS_2 as an active channel material has serious drawbacks including the large contact barrier between the source/drain (S/D) metal electrode and MoS_2 channel and the electron transport hindered by Coulomb scattering and trap charges at the interface between the gate dielectric and MoS_2 in the TFT configuration, in comparison with conventional inorganic semiconductors (*20*). These factors significantly reduce the mobility of MoS_2-based TFTs to $\leq 1\ cm^2\ V^{-1}\ s^{-1}$, which is comparable to that of a-H Si (*21*). This low-mobility value prohibits the integration of MoS_2 TFTs into large-area active-matrix OLED (AM-OLED) displays (*22*–*24*). Although researchers have attempted to improve the carrier mobility of devices by integrating high-*k* dielectric materials such as Al_2O_3 or HfO_2 as a gate dielectric in a conventional manner, there are still significant challenges in satisfying the electrical specification demands of various electronic applications (*25*–*27*).

Here, a TFT device is designed using the Al_2O_3 layer in various ways. This Al_2O_3-capped TFT device leads to reduced contact resistance at the metal/MoS_2 interface and permits the doping of the channel region, which, in turn, reduces the scattering charge impurities and an effective decrease in the interface-trapped charge density via a smooth surface. All these benefits synergistically yield uniform MoS_2 TFT arrays with high mobility, which can efficiently operate OLED pixels on flexible plastic substrates.

RESULTS

The backplane circuitry of a flexible display, comprising an array of transistors responsible for turning the individual OLED pixels ON and OFF, was fabricated using a metal-organic CVD (MOCVD)–grown bilayer MoS_2 film on a 6-μm-thick ultrathin polyethylene terephthalate (PET) substrate (Fig. 1A). The MoS_2 TFT has a top-gate configuration sandwiched between two high-*k* dielectric Al_2O_3 layers, leading to the enhancement of the carrier mobility because the top dielectric Al_2O_3 layer facilitates the doping of the MoS_2 film at the channel and S/D contact regions. Furthermore, the bottom Al_2O_3 layer on the SiO_2/Si substrate reduces the roughness and provides a smooth substrate surface compared with that of bare SiO_2 (Fig. 1B). In particular, in contrast to the conventional device structure of MoS_2 TFTs, in which the S/D electrodes are formed on top of the MoS_2 film, the S/D electrodes of the device are located below the MoS_2 film, which aids the subsequent deposition of the top dielectric Al_2O_3 layer and effectively reduces the contact resistance of the S/D contact regions. The decrease in contact resistance enhances the carrier mobility and facilitates the OLED display operation, which requires a high amount of current (*28*). In the atomic force microscopy and cross-sectional high-resolution

[1]School of Electrical and Electronic Engineering, Yonsei University, Seoul 03722, Republic of Korea. [2]School of Chemical Engineering and Materials Science, Chung-Ang University, Seoul 06974, Republic of Korea.
*These authors contributed equally to this work.
†Corresponding author. Email: sooyoungkim@cau.ac.kr (S.Y.K.); ahnj@yonsei.ac.kr (J.-H.A.)

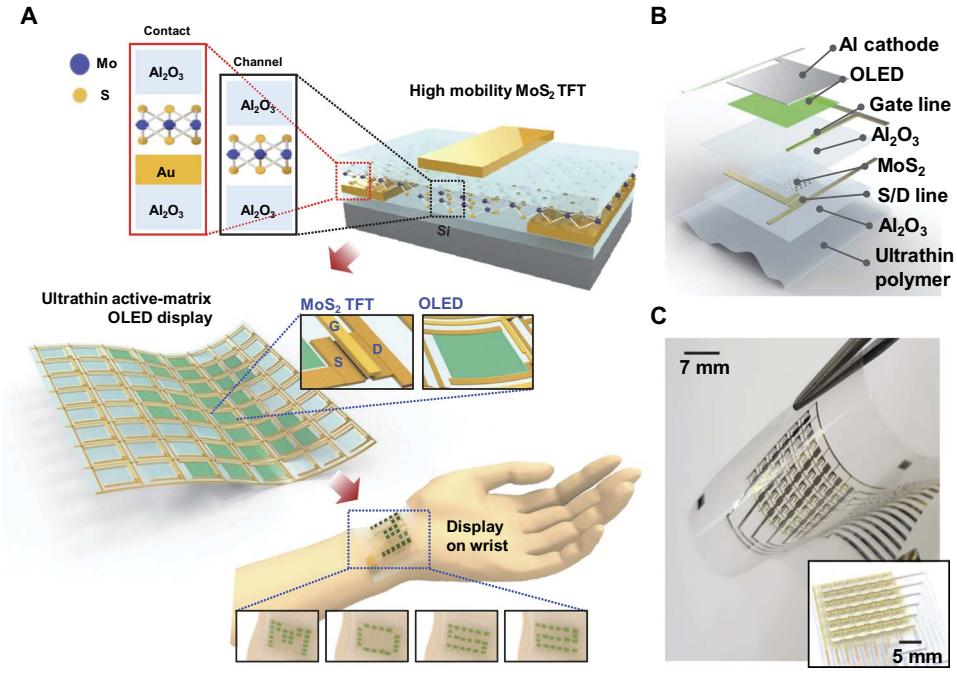

Fig. 1. The device structure of flexible OLED display with MoS_2-based backplane circuitry. (**A**) Schematic of high-mobility MoS_2 TFT using an Al_2O_3 passivation layer. The Al_2O_3 passivation layer ensures n-type doping of not only the MoS_2 channel region but also the contact region (top); ultrathin AM-OLED display using the high-performance MoS_2-based backplane array (middle), which is attached as a display to human skin (bottom). (**B**) Specific layer structure of the ultrathin AM-OLED display. The thickness of the total display system is less than 7 μm. (**C**) Optical image of the assembled display on the flexible ultrathin polymer substrate; low bending stiffness of the display offers ultraflexibility. The inset image shows the flat state of the active-matrix display circuit.

transmission electron microscopy images, improved surface roughness and conformal attachment of the MoS_2 film to the top and bottom Al_2O_3 layers were observed, indicating a clean interface without pinholes or gaps (figs. S1 and S2). The OLED display driven by the bilayer MoS_2-based backplane TFTs was well operated even under bent status or when attached to a human wrist, indicating the possible applications to wearable displays (Fig. 1, A and C) (*28*).

It is crucial to explain the mechanism by which the carrier mobility of bilayer MoS_2 TFTs increases with the use of two dielectric Al_2O_3 layers. The high-*k* Al_2O_3 layer facilitates considerable n-type doping of the MoS_2 layer owing to its oxygen-deficient surface. From earlier studies, band structure calculations have indicated that the presence of interfacial oxygen vacancies in the Al_2O_3 layer lowers the conduction band edge below the Fermi level and initiates the filling of the lower conduction band states of MoS_2 at the interface, leading to the n-type carrier injection in MoS_2 (*25*). Moreover, the large dielectric mismatch at the Al_2O_3/MoS_2 interface suppresses the Coulombic impurities effectively in the MoS_2 layer (*26*). These benefits associated with the presence of a high-*k* dielectric environment possibly enhance the carrier mobility of the resultant MoS_2 TFTs (*27*). The additional advantage of the modified TFT structure is rendered by the bottom Al_2O_3 layer, which provides low surface roughness and further improves the device performance via the suppression of the interface-trapped charge density. The n-type doping owing to the top Al_2O_3 layer in the proposed structure is evident from the Raman and photoluminescence spectra of the bilayer MoS_2 film with different combinations of Al_2O_3 as compared to the bare SiO_2/Si substrate (figs. S3 to S5 and see the Supplementary Materials).

In addition to the damping of the Coulomb scattering and suppression of the interface trap charges, the top Al_2O_3 layer is used for doping MoS_2 in the channel and contact regions in our modified TFT structure. The increased electron concentration at the S/D contact regions reduces the Schottky barrier width, significantly decreasing the contact resistance R_c (fig. S6) (*29*). The decrease in R_c in combination with the doped channel, damped Coulomb scattering, and low surface roughness results in an increase of carrier mobility and uniform output characteristics of the MoS_2 TFTs on a large-area substrate.

To clarify the effect of the top and bottom Al_2O_3 layers to MoS_2 TFT, the devices with each layer and both layers are prepared using MOCVD-grown MoS_2 film (Fig. 2A and table S1). It is evident that back-gate dc characteristics of TFT fabricated on bare SiO_2/Si wafer exhibited a significant improvement in the ON current (②) after Al_2O_3 layer encapsulation, which confirms the doping effect owing to the top Al_2O_3 layer (Fig. 2A). In case of the top gate, a slight increment in the ON current (③) was observed, compared to the back-gate, encapsulated TFT (②), and this increment was further improved (④) for the channel sandwiched between the top and bottom Al_2O_3 layers (Fig. 2A). Here, the bottom Al_2O_3 layer in the sandwiched channel plays a crucial role in reducing the hysteresis significantly owing to the reduction in interface trap charge density (fig. S7 and see the Supplementary Materials). These improved features were also evident in output characteristics and mobility enhancement: a significant boost-up in mobility value (~28 times), positive threshold voltage, V_{th} (~5 V), high ON/OFF ratio (~10^8), and transconductance (1.2×10^{-7} S μm^{-2}) as compared to conventional back-gate structure (Fig. 2, B and C, fig. S8, and table S1). In particular, the positive V_{th} of top-gated TFT can maintain the OFF state of the pixel without the supply of an additional gate bias voltage, which consequently reduces the unnecessary power consumption during the selective pixel operation (table S1). Moreover, there have also been similar effects with MoS_2 single crystal (fig. S9) (*30*, *31*). Thus,

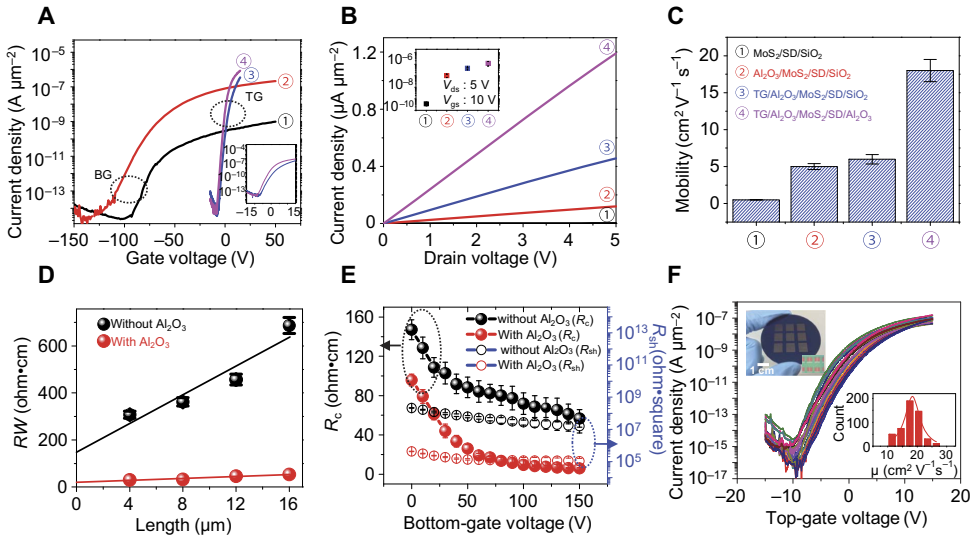

Fig. 2. The device characteristics of MoS_2 TFTs with different structures. (**A**) Transfer characteristics of bilayer MoS_2 TFTs with various device structures (in all cases, MoS_2 was on top of S/D contacts); [inset shows the top-gated (TG) ③ and ④] back-gated (BG) MoS_2 TFT on SiO_2/Si (①), back-gated MoS_2 TFT on SiO_2/Si with Al_2O_3 encapsulation (②), top-gated MoS_2 TFT on SiO_2/Si (③), and top-gated MoS_2 TFT on Al_2O_3/SiO_2/Si (④). The top-gated MoS_2 TFT sandwiched by two Al_2O_3 layers (④) showed the high performance over other fabricated TFTs. (**B**) Output characteristics of all TFTs (①, ②, ③, and ④) corresponding to (A); inset shows the increment of current density at shown bias. (**C**) Mobility values for all TFTs (①, ②, ③, and ④) corresponding to (A). (**D**) Transfer line plot for extracting line contact resistivity (R_c) and channel sheet resistance (R_{sh}) under different gating conditions. (**E**) Extracted R_c (filled circle) and R_{sh} (empty circle) of back-gated bilayer MoS_2 TFTs on Al_2O_3/SiO_2 substrate before (black) and after (red) Al_2O_3 deposition. (**F**) Transfer characteristics of top-gated Al_2O_3/MoS_2/Al_2O_3 sandwiched TFTs (100 devices). Insets show the photograph of wafer-scale fabrication of TFTs and mobility histogram for 500 TFTs showing the average value of mobility (18.1 $cm^2\ V^{-1}\ s^{-1}$).

these characteristics of devices show enough performance capabilities to satisfy the needs of TFT for the operation of the OLED display.

The values of R_c and channel sheet resistance (R_{sh}), which are the important factors influencing the mobility, must be estimated at the S/D/MoS_2 contact region and the MoS_2 channel between the S/D metal electrodes, respectively. The contact properties were characterized as the back-gate dc characteristics of TFTs with and without Al_2O_3 encapsulation. The transfer length method was performed to quantify R_c using TFTs fabricated for the channel lengths of 4, 8, 12, and 16 μm (see the Supplementary Materials). The R_c value, which was calculated as the intercept from the linear fitting of the RW (R, total measured resistance; W, channel width) plot against channel lengths, was 5.9 ± 0.7 ohm·cm and 56.7 ± 9.1 ohm·cm (at V_{gs} = 150 V; V_{ds} = 1 V) for TFTs with and without the Al_2O_3 encapsulation, respectively (Fig. 2D). The R_c value decreased with the increase in the back-gate voltage owing to the electrical doping of MoS_2 with applied gate bias, which reduced the effective barrier height (Fig. 2E) (*32*). R_{sh} remained almost unchanged with the application of back-gate voltages (Fig. 2E); however, a small decrement was observed owing to the increased carrier concentration near the accumulated region for channel formation. In case of top-gate TFTs, there were no significant changes observed in the values of R_c and R_{sh} as compared to back-gate TFTs (Fig. 2E and fig. S10). Notably, R_c and R_{sh} are reduced owing to the presence of the top Al_2O_3-encapsulated layer, leading to significant improvement in the mobility. The above experimental results demonstrate that the top Al_2O_3 dielectric layer effectively doped MoS_2 in both the channel and overlapped contact regions. The doping in the channel region increased the effective carrier concentration, leading to the improved ON current and negative shift in V_{th}, whereas the increased concentration of electrons at the contact region reduced the metal/MoS_2 barrier width, thereby considerably decreasing the values of R_c. Therefore, the improvement in mobility can be attributed to the combined effect of doping in the channel and reduced R_c of the S/D region by the top Al_2O_3 layer. A wafer-scale fabrication (Fig. 2F, inset photograph) of top-gated TFTs resulted in the excellent device yields (>95%), long-term stability (fig. S11), and high uniformity in switching parameters; most of the TFTs showed the high-mobility values (17 to 20 $cm^2\ V^{-1}\ s^{-1}$), low hysteresis (<0.75 V), high ON/OFF ratio (>10^6), and positive V_{th} (5 ± 2 V) (Fig. 2F and fig. S8). Thus, highly reliable and uniform performances of top-gated TFTs render them suitable for use as the backplane of OLED displays.

The performance of a single-OLED pixel connected with a bilayer MoS_2 TFT before the operation of the large-area AM-OLED display was examined (Fig. 3, A and B, and fig. S12). The current density followed the diode characteristics; this observation is evident as OLEDs inherently behave as diodes. The turn-on voltage at 10 cd m^{-2} was 4 V. The luminance linearly increased and reached ≥5000 cd m^{-2} at a voltage greater than 8 V, indicating the excellent emissivity of the fabricated OLED (*33*). The OLED operation was tested by the application of voltage to drive TFT. The representative OLED exhibited excellent emission upon the application of V_{Gate} of approximately 8 V and V_{Data} of approximately 9 V to the gate and drain terminals of the driving TFT, respectively (Fig. 3C). Moreover, with a unit increase in V_{Gate} (4 to 9 V) at a constant V_{Data} of approximately 9 V, the emission intensity of the OLED was distinguishable (Fig. 3D). At V_{Gate} of 9 V, the maximum luminance reached 408 cd m^{-2}; this value is sufficient for display applications, indicating that the fabricated MoS_2 TFT is capable of driving the OLED (*33*). Figure 3E shows the increase in the OLED current (I_{OLED}) against the data bias V_{Data} at different values of V_{Gate}. The value of I_{OLED} in the OFF state remained stable, indicating a leakage-free operation of the driving TFT, whereas, in the ON state, it significantly increased with V_{Gate}. The OLED requires a minimum threshold voltage to turn ON owing to its diode-like behavior. At a low V_{Data} (<5 V), the OLED was turned OFF; therefore, I_{OLED} is independent of V_{Gate}. In

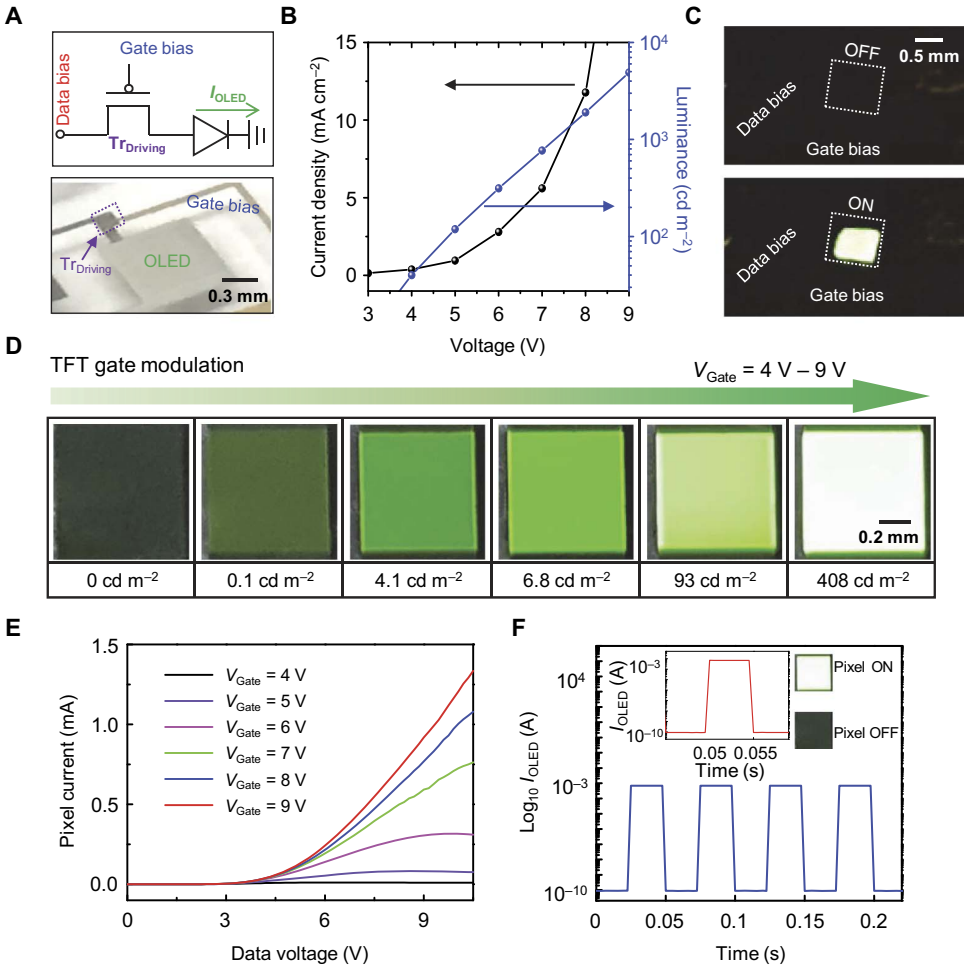

Fig. 3. The device characteristics of an OLED pixel driven by MoS_2 TFT. (**A**) Equivalent circuit diagram (top) and optical image of unit AM-OLED pixel by a single TFT. The single pixel is composed of a transistor and diode for a demonstration of the simplified active-matrix circuitry. (**B**) Current density and luminance of typical OLED device as a function of applying voltage. (**C**) Photographic images of ON/OFF switching using gate bias control of MoS_2 TFT. (**D**) Brightness control of unit OLED pixel according to gate bias. Luminance is well distinguishable as a function of the bias, which is stepped from 4 to 9 V (steps, 1 V). (**E**) Current-voltage (*I-V*) characteristics of the unit pixel during data voltage sweep from 0 to 10 V with gate bias steps. (**F**) Plot of pixel switching properties controlled using gate bias repeatedly. OLED is reliably turned ON and OFF using the MoS_2 TFT gate signal.

contrast, it turned ON at high V_{Data} (≥5 V); thus, I_{OLED} significantly increased with V_{Data} (fig. S13) and demonstrated an apparent V_{Gate} dependency. The OLED exhibited rapid ON and OFF states against a repeated V_{Gate} pulse of ±10 V (Fig. 3F). The response time was estimated to be 2.5 ms, which was limited by the measurement system, but was still sufficiently low to drive the OLED with a short delay time (*3*). All the aforementioned operations of single OLEDs driven by the MoS_2 TFT indicated that the MoS_2 TFT in the developed top-gate configuration successfully drove the OLED unit.

The prototype ultrathin flexible AM-OLED display driven by a bilayer MoS_2-based backplane was demonstrated. The complete assembly (inset of Fig. 4A and fig. S14), including the active-matrix array and deposited OLED units, was arranged on a thin PET sheet (thickness, 6 μm) with the help of polydimethylsiloxane-coated glass carrier substrate (fig. S15). The representative AM-OLED exhibited a thickness of approximately 7 μm, which is thin enough to yield a smaller value of bending stiffness. The MoS_2-based backplane contributes significantly to the realization of a low value of bending stiffness owing to the good mechanical property of the atomically thin MoS_2 layer. Thus, a low value of bending stiffness of resulting device facilitates conformal contact to human skin, and the excellent mechanical endurance of MoS_2 allows the good operation of the device after the attachment (Fig. 4A). The current ON/OFF mapping corresponding to a representative letter "M" showed that all the pixels (6 × 6 array) functioned well with the variation of ON/OFF current (±2%) without any external compensation circuits, indicating the excellent control of the active matrix on the OLED units (Fig. 4B). The AM-OLED display demonstrated a stable performance during continuous operation while being attached to a human wrist (movie S1 and snapshots in Fig. 4C). Four alphanumeric characters—"M," "O," "S," and "2"—were displayed with rapid response to the systematic change of the program codes for each character and real-time control of V_{Gate} and V_{Data}. The AM-OLED display also functioned well without device failure when it was peeled from the carrier glass substrate (movie S2 and Fig. 4D). Furthermore, the AM-OLED display exhibited excellent endurance under repeated bending tests with a bending radius of 0.7 mm, showing small current variation within 10% (fig. S16) (*34*). These small variations in the pixel current were recovered in a flat condition and did not affect the display

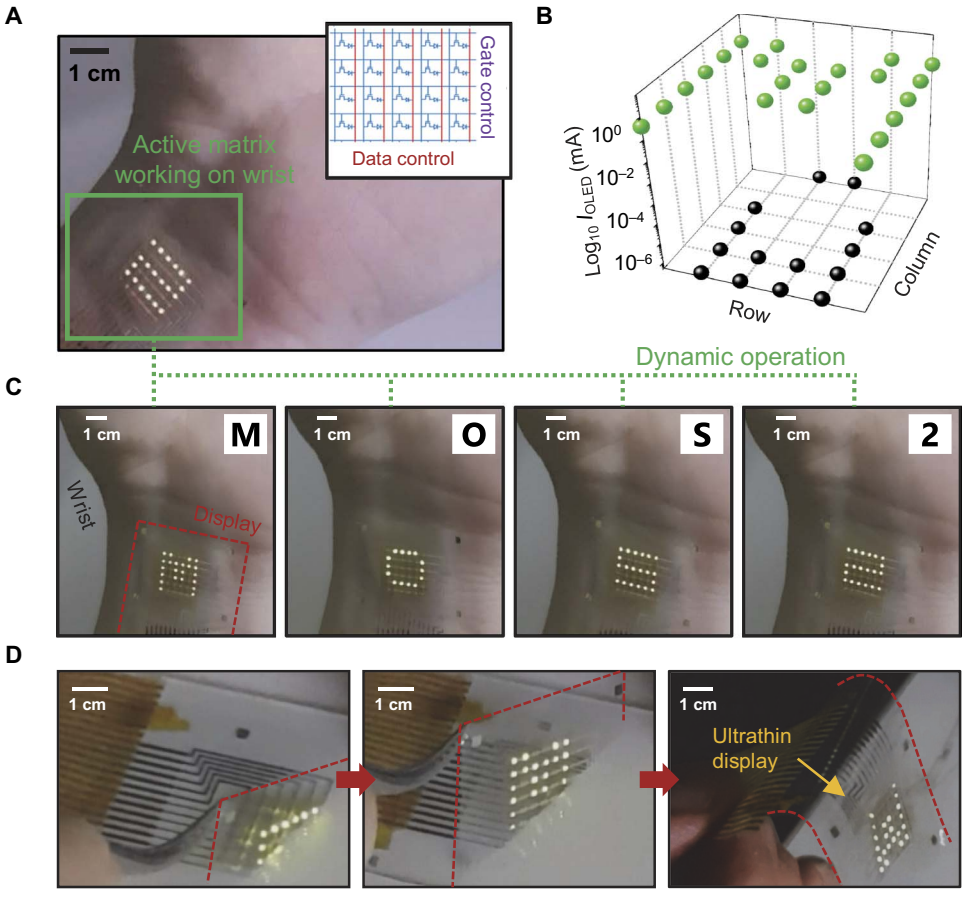

Fig. 4. Flexible OLED display driven by MoS_2 backplane circuitry. (**A**) Photographic image of ultrathin AM-OLED display on the human wrist while the display is operated; display stably attached to the skin owing to the ultrathin substrate. (**B**) Current mapping result during the display of the letter "M"; current of ON pixel (green dot) and OFF pixel (black dot), demonstrating uniform and low cross-talk properties. (**C**) Optical images of dynamic operation on human wrist using the external circuit; representative letters "M," "O," "S," and "2" are sequentially changed on skin according to the active-matrix line addressing. (**D**) Optical images of the peel-off process from carrier glass substrate. The ultrathin display is folded during peel-off, owing to the low bending stiffness of the total display system.

operation. The excellent flexibility of the AM-OLED could be realized owing to the low bending stiffness of the entire AM-OLED assembly.

DISCUSSION

We demonstrated ultrathin flexible OLED displays driven by an active-matrix backplane circuitry composed of MoS_2-based TFTs. The improvement of device properties of TFT was realized by combining the n-type doping of MoS_2 at the S/D and channel regions, damping the Coulomb scattering, and reducing the trap charges and interface scattering through the modified TFT structure with a channel sandwiched between two Al_2O_3 layers. These MoS_2-based TFT arrays were successfully integrated with OLEDs on an ultrathin polymer substrate to demonstrate 6 × 6 active-matrix configurations. The brightness of each pixel was steadily adjusted from 0 to 408 cd m^{-2} via the gate control of the MoS_2-based backplane circuitry, and the uniformity of display was confirmed by the ON/OFF current mapping with fast switching response properties. The flexible AM-OLED display was compatible even in a highly deformed state because it was well operated during the peel-off from the carrier substrate. The results reported here form the basis for the implantation of display-based applications on human movable body parts for wearable health-monitoring electronics, which advance the 2D material-based applications.

MATERIALS AND METHODS

Synthesis of MoS_2

Bilayer MoS_2 was grown using MOCVD. A 4-inch Si wafer with thermally grown 300-nm-thick SiO_2 was placed in a quartz tube with a diameter of 4.3 inch. Before the growth of MoS_2, the wafer was cleaned with water, acetone, and finally isopropanol. Molybdenum hexacarbonyl (MHC; 577766, Sigma-Aldrich) and dimethyl sulfide (DMS; 471577, Sigma-Aldrich), with high equilibrium vapor pressure, were chosen as the Mo and S precursors, respectively, and introduced into the quartz tube using H_2 and Ar as the carrier gases in the gas phase. The optimized parameters for the growth of bilayer MoS_2 included the pressure of 7.5 torr, growth temperature of 550°C, growth time of 20 hours, MHC flow of 1.0 standard cubic centimeter per minute (sccm), DMS flow of 0.3 sccm, Ar flow of 300 sccm, and H_2 flow of 10 sccm.

Fabrication and characterization of MoS_2 TFT

A 50-nm-thick bottom Al_2O_3 layer was deposited on a 300-nm-thick SiO_2 wafer using an atomic layer deposition (ALD) system. S/D electrodes (Cr/Au, 3/30 nm) were patterned on the Al_2O_3/SiO_2 wafer using general photolithography (W/L, 300/4 μm). The bilayer MoS_2 film was transferred onto the wafer and patterned as a channel via reactive ion etching using CHF_3/O_2 plasma. Subsequently, a 50-nm-thick top

Al_2O_3 dielectric layer was deposited on MoS_2. To avoid H_2O molecule traps and the formation of Mo–O bonds during the initial growth cycles of ALD, which significantly degrade the MoS_2 TFT performances, a possible combination of minimum H_2O exposure with low temperature was optimized. In addition, to improve the Al_2O_3/MoS_2 interface, the devices were baked at 110°C overnight under vacuum condition (*35*). Finally, the top-gate electrode (Cr/Au, 3/30 nm) was formed using photolithography and a lift-off process. MoS_2 TFT was characterized using a SourceMeter unit (Keithley 4200 SCS parameter analyzer, Keithley Instruments Inc.).

Fabrication of OLED

The ITO-coated substrate was used to fabricate the Green OLEDs. Prior to it, the substrate was cleaned using acetone, isopropyl alcohol, and deionized water, sequentially followed by drying and exposure to ultraviolet/ozone treatment for 15 min. Subsequently, layers of *N*, *N*′-di(1-naphthyl)-*N*, *N*′-diphenyl-(1,10-biphenyl)-4, 40-diamine (40 nm), tris-(8-hydroxy-quinoline) aluminum (Alq_3, 30 nm), 2, 3, 6, 7-tetrahydro-1, 1, 7, 7,-tetramethyl-1H,5H,11H-10-(2-benzothiazolyl) quinolizine [9,9a,1gh] coumarin (5% doping), bathocuproine (5 nm), and Alq_3 (25 nm) were deposited as the hole transport layer, emitting layer, hole-blocking layer, and electron transport layer under vacuum of approximately 2×10^{-6} Torr at a deposition rate of 1 Å/s. Finally, LiF (1 nm) and Al (100 nm) layers were thermally deposited.

SUPPLEMENTARY MATERIALS

Supplementary material for this article is available at http://advances.sciencemag.org/cgi/content/full/4/4/eaas8721/DC1

Supplementary Text

fig. S1. Atomic force microscopy images of SiO_2 and Al_2O_3/SiO_2.

fig. S2. Cross-sectional transmission electron microscopy image of $Al_2O_3/MoS_2/Al_2O_3$ sandwiched structure.

fig. S3. Optical analysis of MoS_2 film on Al_2O_3 layer.

fig. S4. Optical analysis of MoS_2 film by Al_2O_3 layer encapsulation.

fig. S5. Optical analysis of MoS_2 film sandwiched with Al_2O_3 layer.

fig. S6. Schematic band diagram of Au/MoS_2 contacts with and without Al_2O_3 encapsulation.

fig. S7. Hysteresis of top-gated bilayer MoS_2 TFTs on SiO_2/Si substrate (green) and Al_2O_3/SiO_2/Si substrate (blue).

fig. S8. Statistical data analysis of electrical properties of modified MoS_2 TFT.

fig. S9. Electrical properties of single-crystal MoS_2 TFTs.

fig. S10. Contact and channel sheet resistance analysis of top-gated MoS_2 TFT.

fig. S11. The stability of Al_2O_3-encapsulated MoS_2 TFTs for 1-month period.

fig. S12. Intrinsic OLED properties and structure information.

fig. S13. Analysis of current-voltage characteristics of AM-OLED pixel at different gate biases from 4 to 9 V.

fig. S14. Layout structure of designed active-matrix display.

fig. S15. Schematic illustration of steps for ultrathin AM-OLED display fabrication.

fig. S16. Normalized ON current values of unit pixel at the initial bending radius of 0.7 mm repeatedly.

table S1. The characteristics of MoS_2-based TFTs with different device structures.

movie S1. Active-matrix display operation on human wrist with external circuit.

movie S2. The dynamic operation of ultrathin display during peeling-off process.

Reference (*36*)

REFERENCES AND NOTES

1. M. Kaltenbrunner, T. Sekitani, J. Reeder, T. Yokota, K. Kuribara, T. Tokuhara, M. Drack, R. Schwödiauer, I. Graz, S. Bauer-Gogonea, S. Bauer, T. Someya, An ultra-lightweight design for imperceptible plastic electronics. *Nature* **499**, 458–463 (2013).
2. T. Yokota, P. Zalar, M. Kaltenbrunner, H. Jinno, N. Matsuhisa, H. Kitanosako, Y. Tachibana, W. Yukita, M. Koizumi, T. Someya, Ultraflexible organic photonic skin. *Sci. Adv.* **2**, e1501856 (2016).
3. M. Choi, B. Jang, W. Lee, S. Lee, T. W. Kim, H.-J. Lee, J.-H. Kim, J.-H. Ahn, Stretchable active matrix inorganic light-emitting diode display enabled by overlay-aligned roll-transfer printing. *Adv. Funct. Mater.* **27**, 1606005 (2017).
4. K. Takei, T. Takahashi, J. C. Ho, H. Ko, A. G. Gillies, P. W. Leu, R. S. Fearing, A. Javey, Nanowire active-matrix circuitry for low-voltage macroscale artificial skin. *Nat. Mater.* **9**, 821–826 (2010).
5. B. C.-K. Tee, A. Chortos, A. Berndt, A. K. Nguyen, A. Tom, A. McGuire, Z. C. Lin, K. Tien, W.-G. Bae, H. Wang, P. Mei, H.-H. Chou, B. Cui, K. Deisseroth, T. N. Ng, Z. Bao, A skin-inspired organic digital mechanoreceptor. *Science* **350**, 313–316 (2015).
6. D.-H. Kim, N. Lu, R. Ma, Y.-S. Kim, R.-H Kim, S. Wang, J. Wu, S. M. Won, H. Tao, A. Islam, K. J. Yu, T.-i. Kim, R. Chowdhury, M. Ying, L. Xu, M. Li, H.-J. Chung, H. Keum, M. McCormick, P. Liu, Y.-W. Zhang, F. G. Omenetto, Y. Huang, T. Coleman, J. A. Rogers, Epidermal electronics. *Science* **333**, 838–843 (2011).
7. W. Gao, S. Emaminejad, H. Y. Y. Nyein, S. Challa, K. Chen, A. Peck, H. M. Fahad, H. Ota, H. Shiraki, D. Kiriya, D.-H. Lien, G. A. Brooks, R. W. Davis, A. Javey, Fully integrated wearable sensor arrays for multiplexed in situ perspiration analysis. *Nature* **529**, 509–514 (2016).
8. J. Liang, L. Li, X. Niu, Z. Yu, Q. Pei, Elastomeric polymer light-emitting devices and displays. *Nat. Photonics* **7**, 817–824 (2013).
9. J. Wang, C. Yan, K. J. Chee, P. S. Lee, Highly stretchable and self-deformable alternating current electroluminescent devices. *Adv. Mater.* **27**, 2876–2882 (2015).
10. M. A. McCarthy, B. Liu, E. P. Donoghue, I. Kravchenko, D. Y. Kim, F. So, A. G. Rinzler, Low-voltage, low-power, organic light-emitting transistors for active matrix displays. *Science* **332**, 570–573 (2011).
11. S. Ju, J. Li, J. Liu, P.-C. Chen, Y.-g. Ha, F. Ishikawa, H. Chang, C. Zhou, A. Facchetti, D. B. Janes, T. J. Marks, Transparent active matrix organic light-emitting diode displays driven by nanowire transistor circuitry. *Nano Lett.* **8**, 997–1004 (2008).
12. J. Zhang, Y. Fu, C. Wang, P.-C. Chen, Z. Liu, W. Wei, C. Wu, M. E. Thompson, C. Zhou, Separated carbon nanotube macroelectronics for active matrix organic light-emitting diode displays. *Nano Lett.* **11**, 4852–4858 (2011).
13. F. Bonaccorso, Z. Sun, T. Hasan, A. C. Ferrari, Graphene photonics and optoelectronics. *Nat. Photonics* **4**, 611–622 (2010).
14. G.-H. Lee, Y.-J. Yu, X. Cui, N. Petrone, C.-H. Lee, M. S. Choi, D.-Y. Lee, C. Lee, W. J. Yoo, K. Watanabe, T. Taniguchi, C. Nuckolls, P. Kim, J. Hone, Flexible and transparent MoS_2 field-effect transistors on hexagonal boron nitride-graphene heterostructures. *ACS Nano* **7**, 7931–7936 (2013).
15. K. Kang, S. Xie, L. Huang, Y. Han, P. Y. Huang, K. F. Mak, C.-J. Kim, D. Muller, J. Park, High-mobility three-atom-thick semiconducting films with wafer-scale homogeneity. *Nature* **520**, 656–660 (2015).
16. M. Park, Y. J. Park, X. Chen, Y.-K. Park, M.-S. Kim, J.-H. Ahn, MoS_2-based tactile sensor for electronic skin applications. *Adv. Mater.* **28**, 2556–2562 (2016).
17. S. Yu, J. S. Kim, P. J. Jeon, J. Ahn, J. C. Park, S. Im, Transition metal dichalcogenide-based transistor circuits for gray scale organic light-emitting displays. *Adv. Funct. Mater.* **27**, 1603682 (2017).
18. J. S. Kim, P. J. Jeon, J. Lee, K. Choi, H. S. Lee, Y. Cho, Y. T. Lee, D. K. Hwang, S. Im, Dual gate black phosphorus field effect transistors on glass for NOR logic and organic light emitting diode switching. *Nano Lett.* **15**, 5778–5783 (2015).
19. J. Zhang, H. Yu, W. Chen, X. Tian, D. Liu, M. Cheng, G. Xie, W. Yang, R. Yang, X. Bai, D. Shi, G. Zhang, Scalable growth of high-quality polycrystalline MoS_2 monolayers on SiO_2 with tunable grain sizes. *ACS Nano* **8**, 6024–6030 (2014).
20. A. Allain, J. Kang, K. Banerjee, A. Kis, Electrical contacts to two-dimensional semiconductors. *Nat. Mater.* **14**, 1195–1205 (2015).
21. H. Yabuta, M. Sano, K. Abe, T. Aiba, T. Den, H. Kumomi, K. Nomura, T. Kamiya, H. Hosono, High-mobility thin-film transistor with amorphous $InGaZnO_4$ channel fabricated by room temperature rf-magnetron sputtering. *Appl. Phys. Lett.* **89**, 112123 (2006).
22. H. E. A. Huitema, G. H. Gelinck, J. B. P. H. van der Putten, K. E. Kuijk, C. M. Hart, E. Cantatore, P. T. Herwig, A. J. J. M. van Breemen, D. M. de Leeuw, Plastic transistors in active-matrix displays. *Nature* **414**, 599 (2001).
23. A. D. Franklin, Nanomaterials in transistors: From high-performance to thin-film applications. *Science* **349**, aab2750 (2015).
24. C. Wang, D. Hwang, Z. Yu, K. Takei, J. Park, T. Chen, B. Ma, A. Javey, User-interactive electronic skin for instantaneous pressure visualization. *Nat. Mater.* **12**, 899–904 (2013).
25. A. Valsaraj, J. Chang, A. Rai, L. F. Register, S. K. Banerjee, Theoretical and experimental investigation of vacancy-based doping of monolayer MoS_2 on oxide. *2D Mater.* **2**, 045009 (2015).
26. D. Jena, A. Konar, Enhancement of carrier mobility in semiconductor nanostructures by dielectric engineering. *Phys. Rev. Lett.* **98**, 136805 (2007).
27. Y. Cui, R. Xin, Z. Yu, Y. Pan, Z.-Y. Ong, X. Wei, J. Wang, H. Nan, Z. Ni, Y. Wu, T. Chen, Y. Shi, B. Wang, G. Zhang, Y.-W. Zhang, X. Wang, High-performance monolayer WS_2 field-effect transistors on high-κ dielectrics. *Adv. Mater.* **27**, 5230–5234 (2015).
28. M. S. White, M. Kaltenbrunner, E. D. Głowacki, K. Gutnichenko, G. Kettlgruber, I. Graz, S. Aazou, C. Ulbricht, D. A. M. Egbe, M. C. Miron, Z. Major, M. C. Scharber, T. Sekitani, T. Someya, S. Bauer, N. S. Sariciftci, Ultrathin, highly flexible and stretchable PLEDs. *Nat. Photonics* **7**, 811–816 (2013).
29. D. Kiriya, M. Tosun, P. Zhao, J. S. Kang, A. Javey, Air-stable surface charge transfer doping of MoS_2 by benzyl viologen. *J. Am. Chem. Soc.* **136**, 7853–7856 (2014).

30. A. Sanne, R. Ghosh, A. Rai, H. C. P. Movva, A. Sharma, R. Rao, L. Mathew, S. K. Banerjee, Top-gated chemical vapor deposited MoS_2 field-effect transistors on Si_3N_4 substrates. *Appl. Phys. Lett.* **106**, 062101 (2015).
31. J. Chen, W. Tang, B. Tian, B. Liu, X. Zhao, Y. Liu, T. Ren, W. Liu, D. Geng, H. Y. Jeong, H. S. Shin, W. Zhou, K. P. Loh, Chemical vapor deposition of high-quality large-sized MoS_2 crystals on silicon dioxide substrates. *Adv. Sci.* **3**, 1500033 (2016).
32. W. S. Leong, X. Luo, Y. Li, K. H. Khoo, S. Y. Quek, J. T. L. Thong, Low resistance metal contacts to MoS_2 devices with nickel-etched-graphene electrodes. *ACS Nano* **9**, 869–877 (2015).
33. T. Sekitani, H. Nakajima, H. Maeda, T. Fukushima, T. Aida, K. Hata, T. Someya, Stretchable active-matrix organic light-emitting diode display using printable elastic conductors. *Nat. Mater.* **8**, 494–499 (2009).
34. S. Manzeli, A. Allain, A. Ghadimi, A. Kis, Piezoresistivity and strain-induced band gap tuning in atomically thin MoS_2. *Nano Lett.* **15**, 5330–5335 (2015).
35. J.-G. Song, S. J. Kim, W. J. Woo, Y. Kim, I.-K. Oh, G. H. Ryu, Z. Lee, J. H. Lim, J. Park, H. Kim, Effect of Al_2O_3 deposition on performance of top-gated monolayer MoS_2-based field effect transistor. *ACS Appl. Mater. Interfaces* **8**, 28130–28135 (2016).
36. J. Jeon, S. K. Jang, S. M. Jeon, G. Yoo, Y. H. Jang, J.-H. Park, S. Lee, Layer-controlled CVD growth of large-area two-dimensional MoS_2 films. *Nanoscale* **7**, 1688–1695 (2015).

Acknowledgments

Funding: This work was supported by the National Research Foundation of Korea (NRF-2015R1A3A2066337). **Author contributions:** J.-H.A. planned and supervised the project. S.Y.K. co-supervised the project. B.K.S. advised and supported the project. M.C. and Y.J.P. conducted most of the experiments regarding the device fabrication and characterization. S.-R.B. interpreted the data and supported OLED part experiment. All authors analyzed the data and wrote the manuscript. **Competing interests:** J.-H.A. and Y.J.P. are inventors on a Korean patent application related to this work filed by Yonsei University (10-2017-0055578, 28 April 2017). The authors declare no other competing interests. **Data and materials availability:** All data needed to evaluate the conclusions in the paper are present in the paper and/or the Supplementary Materials. Additional data related to this paper may be requested from the authors.

Submitted 28 December 2017
Accepted 2 March 2018
Published 20 April 2018
10.1126/sciadv.aas8721

Citation: M. Choi, Y. J. Park, B. K. Sharma, S.-R. Bae, S. Y. Kim, J.-H. Ahn, Flexible active-matrix organic light-emitting diode display enabled by MoS_2 thin-film transistor. *Sci. Adv.* **4**, eaas8721 (2018).